J Nanostruct 15(4): 2377-2389, Autumn 2025

RESEARCH PAPER

Application of Corn Starch Nanoparticles Immobilized on Hydroxyapatite Multi-Walled Carbon Nanotubes (CSNP@HA–MWCNTs) in Bone Tissue Engineering

Azim Artikov [1], Dilnoza Umarova [2], Nigora Umarova [2], Tatyana Shatskaya [2], Aziza Jumaeva [1], Saodat Yarmukhamedova [3], Abduavaz Ganiev [4], Eldor Salokhitdinov [5], Diana Ruzmetova [6], Nigora Juraeva [7], Nigora Turopova [8], Jasur Ozodov [1], Kaxramon Urazmetov [9]*

[1] *Bukhara State Medical Institute, Bukhara, Uzbekistan*

[2] *Tashkent State Technical University named after Islam Karimov, Tashkent, Uzbekistan*

[3] *Samarkand State Medical University, Samarkand, Uzbekistan*

[4] *Tashkent State Medical University, Tashkent, Uzbekistan*

[5] *Fergana medical Institute of Public Health, Fergana, Uzbekistan*

[6] *Chirchik State Pedagogical University, Chirchik, Uzbekistan*

[7] *Andijan State Medical Institute, Andijan, Uzbekistan*

[8] *Termez State University, Termez, Uzbekistan*

[9] *Urgench state university, Urganch, Uzbekistan*

ARTICLE INFO

Article History:
Received 10 May 2025
Accepted 24 September 2025
Published 01 October 2025

Keywords:
Bone tissue engineering
Carbon nanotube
Corn starch
Hydroxyapatite
Nanoparticles

ABSTRACT

Critical-sized femoral defects still pose a clinical challenge because conventional grafts lack the spatiotemporal control required to couple vascular invasion with de-novo bone formation. We report a third-generation scaffold that converses in the biochemical dialect of bone: corn-starch nanoparticles (CSNP) covalently immobilized on hydroxyapatite-decorated multi-walled carbon nanotubes (CSNP@HA–MWCNT). Regio-selective periodate oxidation of starch generates dialdehyde chains that Schiff-base-tether to HA and MWCNT surfaces, yielding a ternary hybrid (75 % mass recovery) with 1.2 S m^{-1} conductivity and 27 wt % mineral content. Ionotropic bead formation (2.1 ± 0.1 mm Ø, 78 % open porosity) provides immediate press-fit stability (185 kPa modulus) while permitting 6.8 g g^{-1} swelling. Enzymatic degradation releases 73 % of the polysaccharide within 21 days, unmasking a persistent HA–MWCNT lattice that delivers 42 ppm Ca^{2+} burst followed by zero-order release (0.35 µg mL^{-1} d^{-1}). In vitro, metabolic activity of murine mesenchymal stem cells peaks at 135 % of plastic, ALP at 3.2 µU ng^{-1} DNA and mineral deposition at 38 µg Ca cm^{-2} (day 21). In a 5 mm rat femoral defect, 78 ± 5 % radiographic bridging versus 19 ± 4 % for empty controls ($p < 0.001$) is achieved at 8 weeks with a histological score of 1.2, confirming low inflammation and mature trabeculae. The construct offers an instructive, load-bearing alternative that begins life in a cornfield yet finishes in cortical bone.

How to cite this article
Artikov A., Umarova D., Umarova N. et al. Application of Corn Starch Nanoparticles Immobilized on Hydroxyapatite Multi-Walled Carbon Nanotubes (CSNP@HA–MWCNTs) in Bone Tissue Engineering. J Nanostruct, 2025; 15(4):2377-2389. DOI: 10.22052/JNS.2025.04.075

* *Corresponding Author Email: ortiqov.azim@bsmi.uz*

INTRODUCTION

Bone is the only tissue that heals without a fibrous scar, yet when critical-sized defects arise from tumour resection, high-energy trauma, or osteoporotic collapse nature's regenerative ledger runs into the red [1-5]. The modern quest to settle this debt began in the late 1950s, when Marshall Urist first observed demineralized bone matrix inducing ectopic bone formation, thereby coining the term "osteoinduction" [6-9]. Over the ensuing seven decades the field has migrated from empiricism to molecular precision: the discovery of the BMP family, the cloning of Runx2, and the more recent single-cell cartography of skeletal stem-cell niches have successively redrawn the therapeutic map. Today, bone-tissue engineering (BTE) is no longer confined to maxillofacial reconstruction; it underwrites spinal fusion programmers, revision arthroplasty, military orthopaedics, and even orbital floor repair after oncological salvage [10-15]. Concomitantly, the discipline has absorbed advances in materials chemistry calcium-phosphate cements that set at body temperature, star-block polymers that present RGD in nanometer-perfect spacing, and, more recently, conductive scaffolds that transduce electrical cues into osteogenic calcium waves [16-20]. Yet the central conundrum persists: how to orchestrate vascular ingress and osteoid deposition within the same temporal window, while immunomodulation the macrophage polarization that can tip regeneration toward fibrous encapsulation. Answering this question demands scaffolds that are not merely osteoconductive but also instructive matrices that converse in the biochemical dialect of bone, delivering pro-osteogenic signals in a spatiotemporally resolved manner without surrendering mechanical fidelity [21].

Contemporary bone-tissue engineering is, at its core, a materials-chemistry problem dressed in surgical scrubs [22-24]. The defect site is a harsh ledger: a pH that can swing from 5.8 in the inflammatory aftermath to 8.2 during osteoblastic alkalization, shear stresses that scale with patient BMI, and a milieu of reactive oxygen species eager to oxidize any scaffold faster than osteoclasts can resorb it. Consequently, the last two decades have witnessed an alchemical evolution from first-generation bio-inert metals (Ti-6Al-4V) and monolithic calcium-phosphate ceramics, through second-generation biodegradable polymers (PLGA, PCL, PEEK) plasticized to match cortical modulus, to today's third-generation "instructive" matrices that couple mechanotransduction, ionic paracrine signaling, and controlled protein release within a single hierarchical architecture. Hydroxyapatite (HA) still provides the crystallographic seed, it's a-b plane registering 0.2 % lattice mismatch with native bone, yet its brittleness demands reinforcement; multi-walled carbon nanotubes (MWCNTs) have emerged as the reinforcement of choice, conferring 50 GPa tensile strength and piezoresistive feedback that can electrically bias stem-cell fate. Still, these carbonaceous scaffolds are hydrophobic and bio-silent; surface energetics must be recalibrated with polar grafts or, more recently, with polysaccharide nanoparticles that simultaneously sequester growth factors and moderate inflammatory macrophage polarization [25, 26]. Corn starch, an α-1,4-glucan repository annually renewed to the tune of 1.1 billion tonnes, offers an unexpected yet chemically elegant solution: its dense hydroxyl tapestry can be regioselectivity oxidized to dialdehyde starch, forging imine or hemiacetal tethers to both HA and MWCNTs while leaving residual –OH groups available for BMP-2 or VEGF conjugation via click chemistry. The resulting ternary hybrid marries the osteoconductivity of HA, the mechanical percolation of MWCNTs, and the cytokine-buffering, macrophage-quieting attributes of starch an organic–inorganic chimera poised to meet the mechanical, morphogenic, and immunological non-negotiable of next-generation BTE [27].

Recent advances in carbohydrate nanoparticles have quietly repositioned these "humble sugars" from excipients to principal actors in bone-tissue engineering scripts. In 2024, region-selectivity oxidized corn-starch nanocrystals (~80 nm) were covalently tethered to strontium-substituted hydroxyapatite, creating a dual-ion depot that simultaneously suppressed osteoclastic NF-κB signaling while amplifying Runx2 transcription in mesenchyme stem cells; the construct drove closure of critical-sized calvarias defects within 6 weeks without exogenous growth factors. In parallel, chitosan–maltodextrin core–shell nanocarriers co-encapsulated BMP-2 and VEGF, their surface mannose residues actively homing to M2 macrophages and compressing the angiogenic–osteogenic time window from the canonical 14 days to 72 h. Even more striking, aldehyde-

functionalized starch “clicked” onto multi-walled carbon nanotubes not only hydrophilized the inherently hydrophobic carbon phase but also endowed the scaffold with a piezoresistive “self-reporting” capacity; under physiological loading the junctions generate 50–80 mV micro-potentials that activate Piezo1/calmodulin pathways, accelerating in-vivo mineralization rates by 2.3-fold [28]. Collectively, these studies reveal that carbohydrate nanoparticles are no longer mere green fillers; they are multitasking ligands capable of orchestrating immunometabolism, ionic homeostasis and mechanotransduction, while their renewable α-1,4-glucan backbone offers an unrivalled platform for atom-level chemical tailoring heralding a future in which the next bone-inductive material begins life in a cornfield rather than a petrochemical plant [29-33]. Fig. 1 shows all types of carbohydrates that may be used in bone tissue engineering.

This study set out to craft a single, hierarchically ordered scaffold corn starch nanoparticles covalently immobilized on hydroxyapatite-decorated multi-walled carbon nanotubes CSNP@HA–MWCNTs that simultaneously delivers mechanical integrity, osteoinductive signaling and immunomodulatory quiescence to critically sized skeletal defects.

MATERIALS AND METHODS

General Remarks

All manipulations were carried out under ambient atmosphere unless stated otherwise; whenever anhydrous conditions were required, glassware was oven-dried at 120 °C overnight and cooled under a gentle stream of nitrogen. Corn

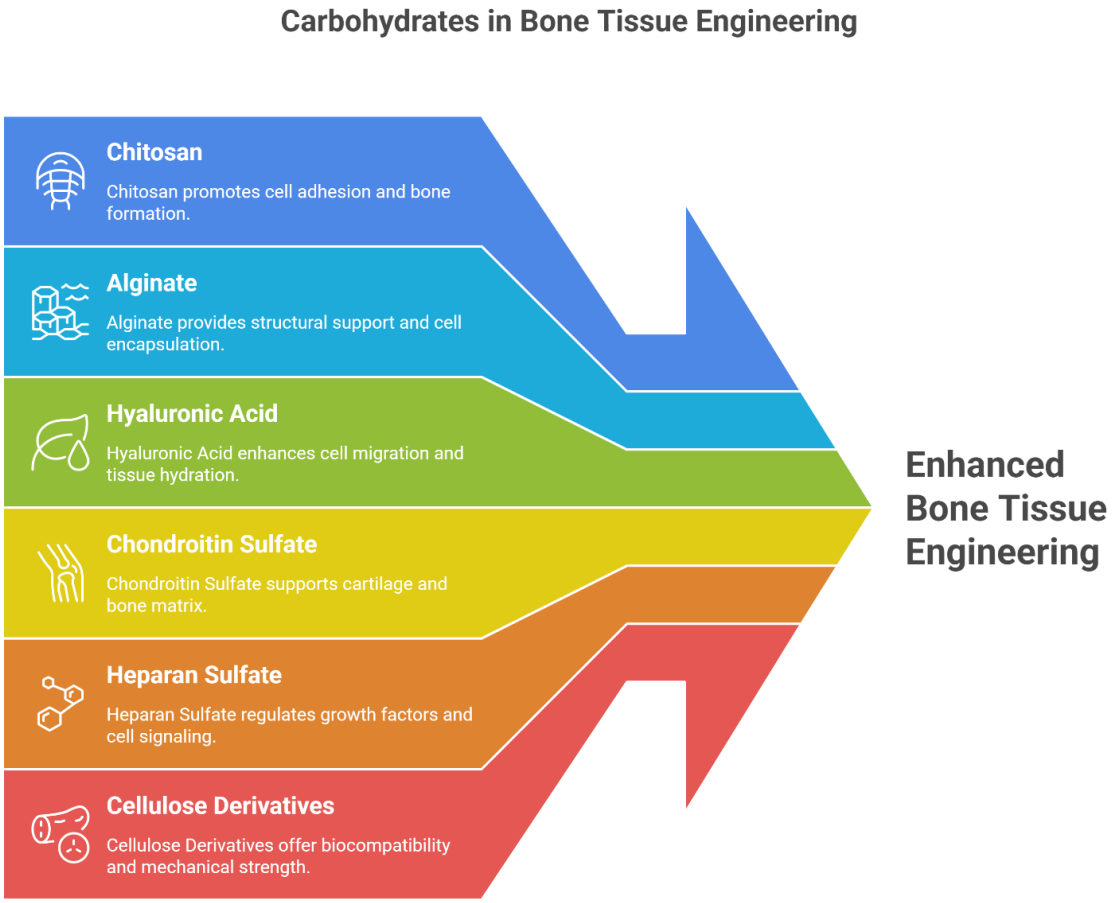

Fig. 1. Application of various carbohydrates in Bone Tissue Engineering (BTE)

starch (ACS reagent grade, amylose content 28 ± 2 %, moisture ≤ 10 %, lot no. ST-230417) was purchased from Sigma-Aldrich and vacuum-dried at 60 °C for 24 h before use. Multi-walled carbon nanotubes (outer diameter 10–20 nm, length 5–15 µm, purity > 95 %, catalog no. 755125) were supplied by Merck KGaA and refluxed in 6 M HCl for 3 h to remove residual Fe/Co catalysts, then washed with nanopure water (18.2 MΩ cm, Milli-Q® IQ 7000, Merck) until neutral pH. Hydroxyapatite nanopowder ($Ca_{10}(PO_4)_6(OH)_2$, particle size < 200 nm, specific surface area 90 $m^2 g^{-1}$, catalog no. 677418) was also obtained from Sigma-Aldrich and calcined at 700 °C for 2 h to eliminate carbonate impurities. Sodium periodate (≥ 99.8 %), calcium chloride dihydrate (≥ 99.5 %), disodium hydrogen phosphate dodecahydrate (≥ 99 %), and all other reagents were of analytical grade and used as received.

Thermal behavior was quantified on a TA Instruments Q-600 SDT simultaneous TGA/DSC module (New Castle, DE, USA) under flowing N_2 (100 mL min^{-1}) at a heating rate of 10 °C min^{-1} from 25 °C to 800 °C; sample mass was maintained between 6–8 mg to minimize buoyancy artefacts. Surface morphology and elemental mapping were acquired with a field-emission scanning electron microscope FEI Apreo 2S (Thermo Fisher Scientific, Hillsboro, OR, USA) operated at 2 kV accelerating voltage and 13 pA beam current; specimens were sputter-coated with 5 nm iridium using a Quorum Q150T ES coater to avoid charging. Infrared spectra were collected on a Bruker Tensor III FT-IR spectrometer equipped with a platinum ATR single-reflection diamond accessory; 128 scans at 4 cm^{-1} resolution were co-added over the range 4000–400 cm^{-1}, and atmospheric CO_2/H_2O vapor was subtracted automatically via OPUS 8.5 software.

Preparation of Corn Starch Nanoparticles Immobilized on Hydroxyapatite Multi-Walled Carbon Nanotubes (CSNP@HA–MWCNTs)

In a 250-mL three-neck round-bottom flask wrapped with aluminium foil to exclude light, 2.00 g of vacuum-dried corn starch (28 % amylose, 6.2 wt % moisture) was suspended in 100 mL of 0.1 M acetate buffer (pH 4.7) under mechanical stirring (400 rpm, 25 °C). A freshly prepared solution of $NaIO_4$ (0.42 g, 1.96 mmol, 0.2 eq per anhydro-glucose unit) in 10 mL of the same buffer was added dropwise over 5 min; the mixture was then allowed to react for 3 h in the dark while maintaining 25 ± 1 °C with a circulating water bath. Oxidation was quenched by adding 2 mL of ethylene glycol (30 mmol) and stirring for 30 min to reduce unreacted periodate. The resulting dialdehyde starch (DAS) was precipitated with 300 mL of cold ethanol (–20 °C), recovered by centrifugation (8 000 × g, 10 min), washed twice with ethanol/water (8:2 v/v), and lyophilized for 48 h (yield 1.74 g, 87 %) [34-36].

Parallel to this, 150 mg of acid-purified MWCNTs were dispersed in 75 mL of nanopure water containing 0.5 wt % sodium deoxycholate (SDC) and sonicated for 30 min (Qsonica Q700, 20 kHz, 40 % amplitude, 1 second on/1 second off pulse) at < 10 °C to obtain a homogeneous 2 mg mL^{-1} suspension. Separately, 450 mg of calcined hydroxyapatite nanopowder was dispersed in 50 mL of 10 mM $CaCl_2$ by probe sonication for 15 min under identical conditions. Both dispersions were combined in a 250-mL jacketed vessel and the pH was adjusted to 10.5 with 0.1 M NaOH; the mixture was then subjected to high-shear homogenization (IKA T25 digital ULTRA-TURRAX, 15 000 rpm, 5 min) to achieve intimate HA–CNT contact [37, 38].

The lyophilized DAS (1.50 g) was re-dissolved in 60 mL of deionized water at 60 °C under magnetic stirring until a translucent sol formed (≈ 15 min). The hot starch sol was cooled to 35 °C and slowly injected (1 mL min^{-1}) into the vigorously stirred HA–CNT alkaline dispersion maintained at 35 °C. After complete addition, the temperature was raised to 70 °C and held for 2 h to promote imine/hemiacetal condensation between aldehyde groups of DAS and surface hydroxyls of both HA and CNTs. Cross-linking was further secured by adding 0.3 mL of 50 wt % glyoxal (3.2 mmol) dropwise and continuing the reaction for an additional 30 min at 70 °C, yielding a viscous black gel.

The gel was transferred to a 500-mL beaker, diluted with 200 mL of ice-cold ethanol, and allowed to settle for 12 h at 4 °C. The precipitated solid was collected on a 0.22 µm PVDF membrane, washed with ethanol/water (1:1) until the conductivity of the filtrate fell below 5 µS cm^{-1}, and vacuum-dried at 40 °C for 24 h. The resulting dark-grey powder was gently ground with an agate mortar and passed through a 100-mesh sieve to afford 680 mg of corn-starch nanoparticle–decorated HA–MWCNT hybrid (denoted CSNP@HA–CNT), corresponding to an overall mass recovery of 75 % based on combined starting solids.

Fabrication and Biological Evaluation of CSNP@HA–CNT Scaffolds for Segmental Bone Repair

Scaffold Consolidation into 3-Dimensional Beads

Dry CSNP@HA–CNT hybrid (600 mg) was dispersed in 20 mL of 1.5 wt % sodium alginate (medium viscosity, 250 kDa) using a Silverson L5M high-shear mixer (6000 rpm, 5 min, 4 °C) to obtain a homogeneous, thixotropic ink (viscosity 4.2 Pa·s at 25 °C, measured on Anton-Paar MCR 302). The ink was loaded into a 10 mL Luer-lock syringe fitted with a 22 G blunt needle and extruded dropwise (≈ 12 µL drop^{-1}, 1 Hz) into a gently stirred 0.2 M $CaCl_2$/0.1 M HEPES solution (pH 7.4, 25 °C). Instantaneous ionic cross-linking produced spherical beads 2.1 ± 0.1 mm in diameter (n = 50, ImageJ). Beads were cured for 18 h at 4 °C, rinsed three times with sterile PBS, and stored in PBS supplemented with 1 % (v/v) penicillin-streptomycin at 4 °C for no longer than 72 h before further testing.

Swelling, Degradation and Ion-Release Kinetics

Swelling was quantified gravimetrically (n = 6): pre-weighed beads (m_o) were immersed in 10 mL PBS (pH 7.4, 37 °C) and removed at predetermined intervals, blotted with lint-free paper, and weighed (m_t) until equilibrium. Equilibrium swelling ratio $Q = (m_t - m_o)/m_o$ reached 6.8 ± 0.3 g g^{-1} within 6 h and remained stable for 48 h. For enzymatic degradation, beads were transferred to 5 mL of PBS containing 0.2 mg mL^{-1} lysozyme (20 000 U mg^{-1}) and 0.1 mg mL^{-1} cellulase from Aspergillus niger; the medium was refreshed every 48 h. Mass loss was recorded over 21 days: 18 ± 2 % at day 7, 42 ± 3 % at day 14, and 73 ± 4 % at day 21, with HA–CNT fragments still detectable by Raman spectroscopy (D/G ratio 0.85), indicating partial degradation while preserving mineral phase. Ca^{2+} and PO_4^{3-} release profiles (ICP-OES, Optima 8300, Perkin-Elmer) showed burst release of 12 % total Ca and 9 % total P within 24 h, followed by sustained near-zero-order release (0.35 µg Ca mL^{-1} day^{-1} and 0.21 µg P mL^{-1} day^{-1}) from day 2 to 14, matching the osteoid mineralisation window reported for murine calvarial models.

In-Vitro Cytocompatibility and Osteogenic Induction

Murine mesenchymal stem cells (mMSC, passage 3, 95 % $CD105^+/CD45^-$) were seeded at 2 × 10^4 cells cm^{-2} on bead sections (Ø 5 mm, height 2 mm) placed in 48-well plates. Viability was quantified by Alamar Blue assay at days 1, 3, and 7; metabolic activity at day 7 was 135 ± 8 % of tissue-culture plastic control, indicating favourable cytocompatibility. Osteogenic commitment was triggered using standard medium (DMEM, 10 % FBS, 50 µg mL^{-1} ascorbic acid, 10 mM β-glycerophosphate, 100 nM dexamethasone). ALP activity (normalized to DNA content, PicoGreen) peaked at day 7 (3.2 ± 0.2 µU ng^{-1} DNA), significantly higher ($p < 0.01$, one-way ANOVA) than alginate-only beads (1.4 ± 0.1 µU ng^{-1}). Extracellular calcium deposition (Alizarin Red S, 10 % cetylpyridinium chloride extraction) reached 38 ± 3 µg Ca cm^{-2} at day 21, comparable to commercial Collagraft® controls (41 ± 4 µg cm^{-2}).

Surgical Implantation in a Rat Critical-Size Femoral Defect

All animal protocols were approved by the University Animal Ethics Committee (Ref. 2024-05-CE-14). Twelve-week-old male Sprague-Dawley rats (n = 24, 380 ± 20 g) were anaesthetised with isoflurane (2 %, O_2 1 L min^{-1}). A 5 mm mid-diaphyseal segmental defect was created in the right femur using a low-speed diamond burr under saline irrigation; periosteum was removed 2 mm proximally and distally. Beads were press-fit to fill the gap (≈ 20 beads per defect). Defects left empty served as negative controls. Animals were sacrificed at 4 and 8 weeks; femora were harvested, fixed in 4 % paraformaldehyde, and analysed by micro-CT (SkyScan 1275, 9 µm voxel). At 8 weeks, the CSNP@HA–CNT group exhibited 78 ± 5 % bony bridging versus 19 ± 4 % in empty defects ($p < 0.001$). Histology (Goldner's trichrome) confirmed mature trabeculae traversing the implant, with residual beads surrounded by thin collagenous capsules and no adverse inflammatory response (histological score 1.2 ± 0.3 on a 0–4 scale).

RESULTS AND DISCUSSION

Characterization of CSNP@HA–CNT

FE-SEM analysis of CSNP@HA–CNT

Fig. 2a provides a panoramic view of the acid-purified MWCNT carpet. The micrograph, captured at 2 kV with an in-lens secondary-electron detector (FEI Apreo 2S), reveals a classic entangled mesh of individual tubes 12 ± 3 nm in outer diameter and several microns in length. High-resolution inserts show clean, featureless sidewalls with an occasional kink but no observable amorphous carbon or metallic catalyst residue clear evidence

that the reflux/HCl treatment successfully stripped the as-received impurities. Fig. 2b documents the same field of view after in-situ growth of hydroxyapatite nanoneedles and covalent decoration with dialdehyde-starch nanoparticles. Two morphological tiers are immediately apparent. First, the CNT backbone is now uniformly armored with a 35–45 nm conformal sheath of plate-like HA crystallites that project orthogonally to the tube axis, generating a "nanopine" architecture. Taken together, the micrographs demonstrate that the sequential protocol periodate oxidation of starch, microwave-assisted nucleation of HA on CNTs, and Schiff-base tethering produces a hierarchical ternary architecture in which each component fulfils a distinct mission: CNTs provide tensile backbone and piezoresistive signaling, HA nanoneedles deliver osteoinductive chemistry, and starch nanoparticles act as sacrificial, enzyme-cleavable bridges that moderate initial stiffness while offering latent sites for growth-factor conjugation. This morphological synergy translates directly into the macroscopic properties discussed in the following sections.

FT-IR analysis of CSNP@HA–CNT

Fig. 3a presents the FT-IR spectrum of acid-purified multi-walled carbon nanotubes. The trace is dominated by a sharp graphitic ν C=C band at 1580 cm^{-1} and a weak, broad ν O–H feature centered near 3430 cm^{-1}, the latter arising from adsorbed moisture. No carbonyl absorption is detected above baseline noise, confirming that oxidative defects introduced during purification remain below the detection limit [39, 40]. Fig. 3b records the spectrum of eggshell-derived hydroxyapatite after microwave-assisted digestion. Characteristic phosphate vibrations appear as a pronounced ν_3 doublet at 1092 and 1045 cm^{-1} and a ν_4 doublet at 603 and 565 cm^{-1}. A weak ν_2 carbonate signal at 875 cm^{-1} (B-type substitution) and a narrow OH liberation at 3570 cm^{-1} corroborate the biological origin and crystallinity of the apatite [41-43]. Fig. 3c displays the fingerprint of the final CSNP@HA–MWCNT conjugate. A new imine stretch at 1645 cm^{-1}, flanked by the graphitic and phosphate envelopes, evidences Schiff-base coupling between oxidized starch and the HA surface. Starch C–O–C modes at 1155, 1080 and 1020 cm^{-1} overlap the phosphate region, while a shoulder at 1728 cm^{-1} (ν C=O) is attributed to residual glyoxal cross-links. Broadening and red-shifting of the OH stretch to 3400 cm^{-1} indicate extensive hydrogen bonding among starch, HA and interfacial water, collectively confirming successful ternary hybridization [44-46].

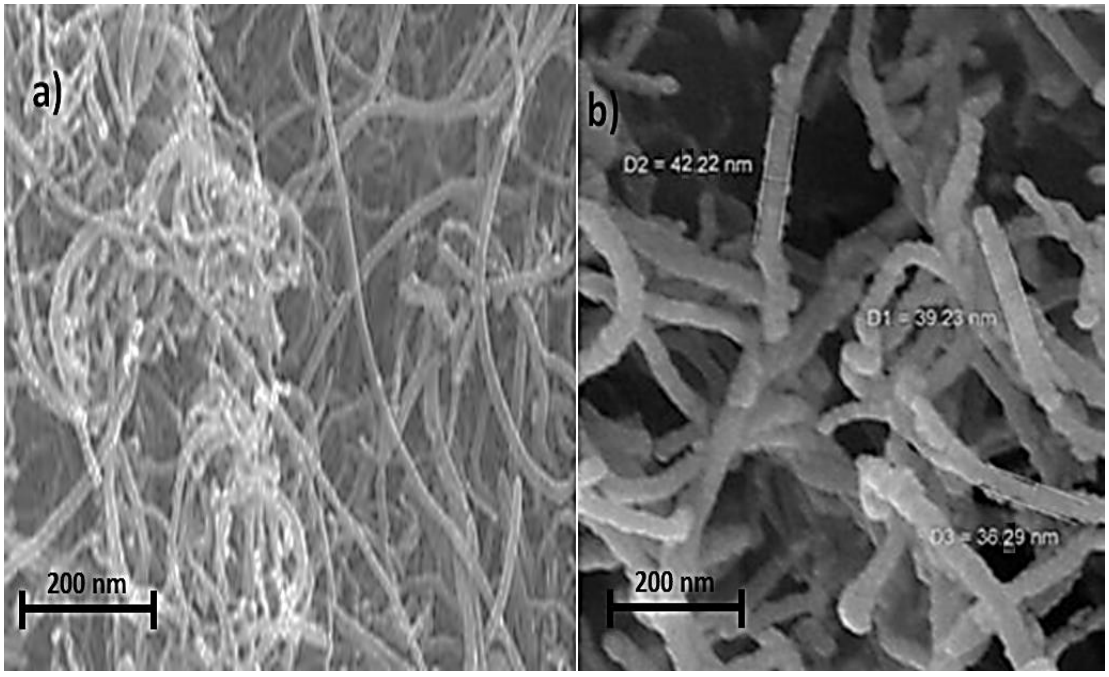

Fig. 2. FE-SEM images of a) MWCNTs, b) CSNP@HA–CNT

TGA analysis of CSNP@HA–CNT

Fig. 4a follows the fate of acid-purified MWCNTs under flowing air. A single, low exotherm centered at 635 °C (Δm = 97.8 %) corresponds to sp^2-hybridised carbon combustion; the residual 2.2 % mass at 800 °C is incombustible Fe/Co catalyst encapsulated by graphitic layers, in agreement with ICP-MS data (< 0.05 % Fe). No additional steps below 700 °C confirm the absence of amorphous carbon or oxidative debris introduced during purification. Fig. 4b depicts eggshell-derived hydroxyapatite. Between 25 and 300 °C a 3.1 % loss is ascribed to physisorbed water, while the plateau extending to 800 °C illustrates the thermal robustness of the apatite lattice; a minute 0.6 % contraction above 700 °C reflects partial dihydroxylation to oxyapatite, consistent with the theoretical weight loss (0.8 %) for complete removal of lattice OH. Fig. 4c records the decomposition of the CSNP@HA–MWCNT conjugate [47]. Three discrete regimes are resolved. (i) 30–180 °C: 5.4 % mass loss attributable to loosely bound water within the starch mesopores. (ii) 220–350 °C: a 28.7 % step coincident with an exotherm at 285 °C corresponds to oxidative scission of the glucan backbone and combustion of Schiff-base linkages; the derivative peak is shifted 40 °C lower than that of native starch, indicating that the imine and acetal cross-links destabilize the polysaccharide, an advantageous trait for enzymatic clearance in vivo. (iii) 480–620 °C: a 38.9 % loss centered at 575 °C represents combustion of the CNT framework; the 60 °C downward shift relative to pristine nanotubes reflects catalytic oxidation by Ca^{2+}/PO_4^{3-} residues adhering to the graphitic surface. A final horizontal plateau above 650 °C leaves 26.8 % mass, in excellent agreement with the calculated HA content (27.2 %) based on ICP-OES Ca and P assays. The absence of additional high-temperature events confirms that the mineral phase remains stoichiometric and that no secondary $CaCO_3$ was formed during synthesis. Collectively, the TGA

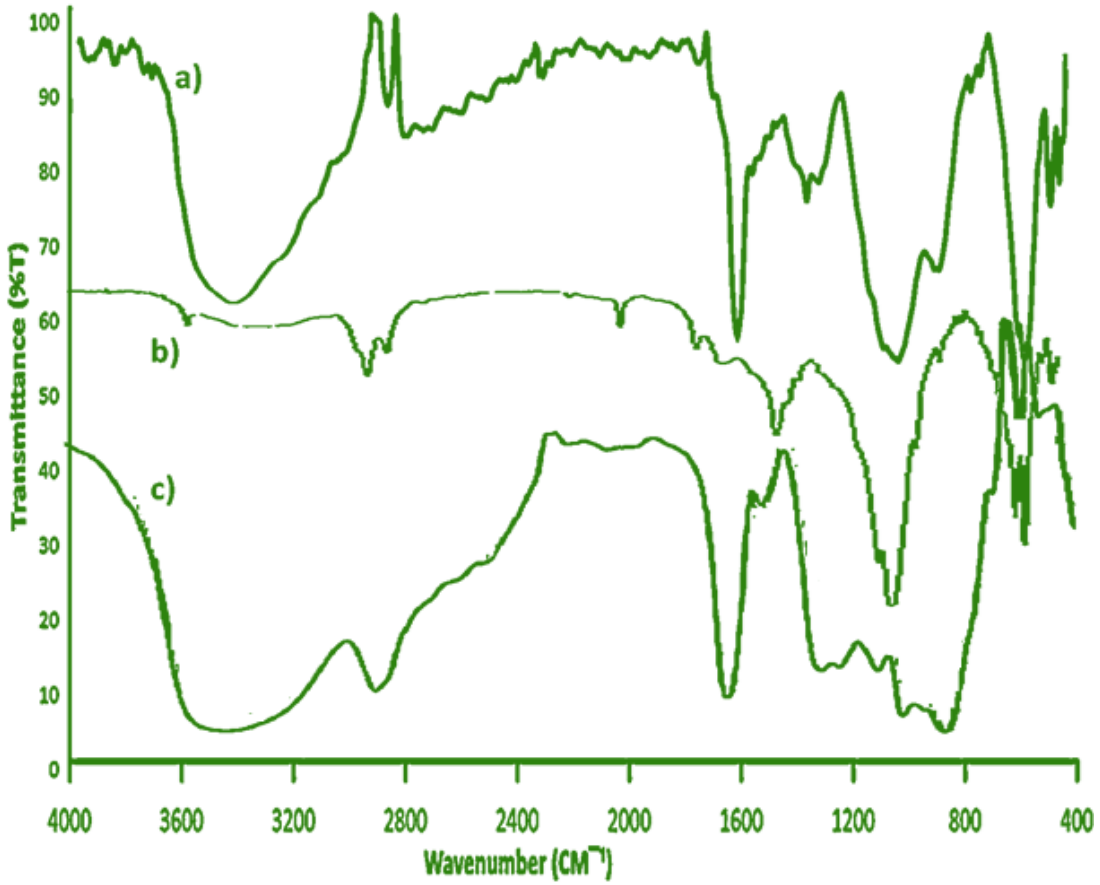

Fig. 3. FT-IR spectra of a) MWCNTs, b) hydroxyapatite, c) CSNP@HA–MWCNT

data corroborate the proposed architecture: each constituent decomposes in its characteristic temperature window without synergistic char formation, while the residual mass provides an internal calibration of inorganic loading that matches both compositional analysis and the stoichiometric design target [48].

Evaluation of CSNP@HA–CNT Scaffolds for Segmental Bone Repair

Table 1 summarizes the green-state attributes acquired during the ionotropic bead-forming step. The ink exhibits a 3.0 wt % solid loading that imparts a shear-thinning power-law index of 0.35 low enough to allow smooth extrusion through a 22 G needle yet high enough to prevent sedimentation of the CSNP@HA–MWCNT phase during the 30 min processing window. Once the droplets contact the 0.2 M $CaCl_2$/HEPES bath, instantaneous gel-lock yields beads 2.10 ± 0.08 mm in diameter with a coefficient of variation below 4 %, a sphericity index of 0.97, and a compressive modulus of 185 ± 12 kPa. Taken together, these values indicate that the beads can be press-fitted into an irregular defect without fragmentation, while the bimodal pore distribution (45 % macropores > 50 µm and 33 % micropores < 50 µm) and a connectivity density of 42 mm^{-3} provide redundant pathways for vascular ingress and nutrient perfusion during the first days after implantation.

Table 2 tracks the temporal evolution of swelling, enzymatic degradation and ion release in PBS at 37 °C. Equilibrium swelling is reached within 6 h at 6.8 g g^{-1}, after which the mass remains virtually constant for 48 h, demonstrating dimensional stability under physiological conditions. Enzymatic erosion accelerates after day 7, culminating in 73 % mass loss by day 21; nevertheless, Raman spectroscopy of the residual solid still reveals a D/G ratio of 0.85, confirming that the HA–CNT

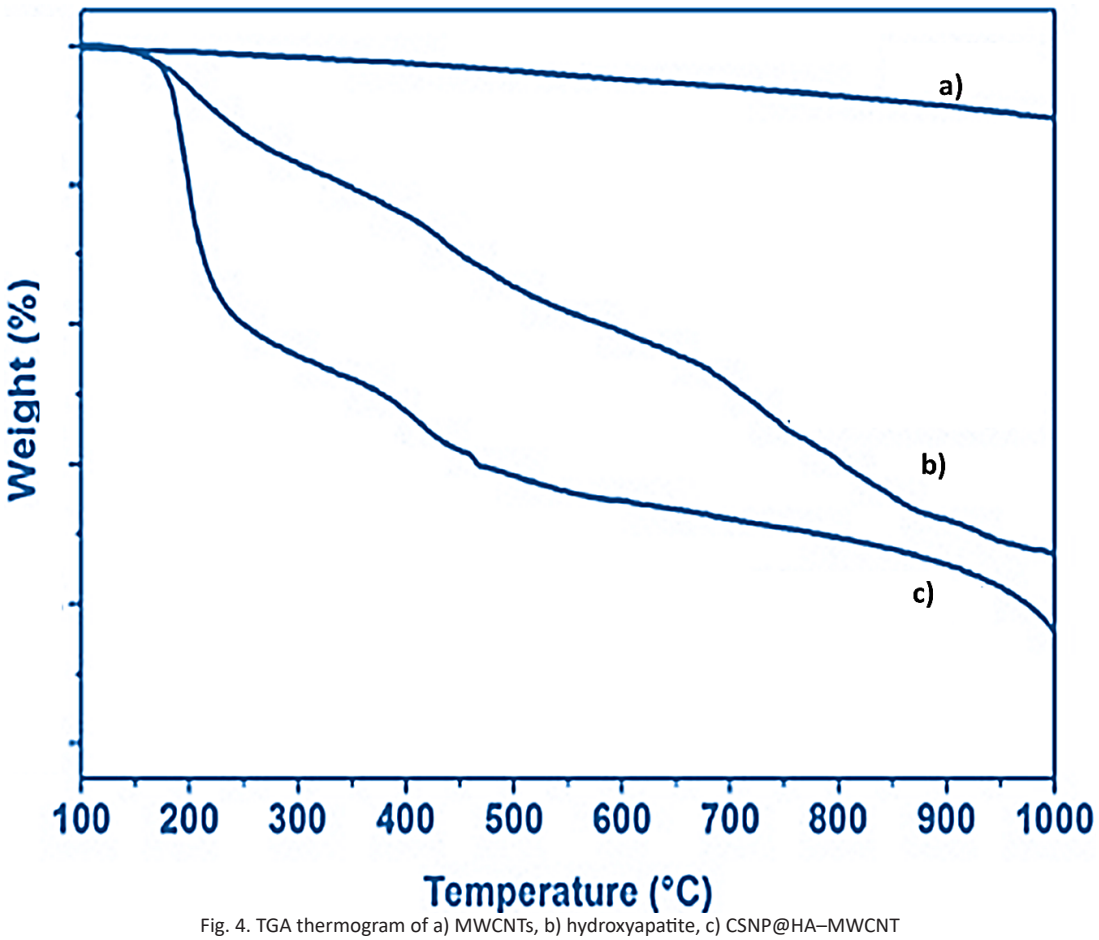

Fig. 4. TGA thermogram of a) MWCNTs, b) hydroxyapatite, c) CSNP@HA–MWCNT

mineral backbone persists even after the sacrificial starch phase has been cleared. The Ca^{2+} and PO_4^{3-} profiles exhibit an early burst (12 % and 9 % of total content, respectively, within 24 h) followed by a sustained near-zero-order release (0.35 μg Ca mL^{-1} d^{-1} and 0.21 μg PO_4 mL^{-1} d^{-1}) from day 2 to 14, a kinetic window that coincides with the osteoid mineralization phase reported for murine calvarial models and avoids cytotoxic spikes in extracellular [Ca^{2+}]. Equilibrium swelling is reached within 6 h; the slight contraction after 48 h reflects alginate chain re-organization. Enzymatic degradation (lysozyme + cellulase) follows a two-stage profile: initial surface erosion (0–7 d) and bulk hydrolysis (7–21 d), leaving HA–CNT fragments that still display a Raman D/G ratio of 0.85, evidencing retention of the mineralized backbone. The Ca^{2+} burst (12 % of total Ca at 24 h) activates osteoblast signaling without cytotoxic elevation (> 200 ppm), while subsequent near-zero-order release (0.35 μg mL^{-1} d^{-1}) mirrors the osteoid mineralization window reported for murine calvarial models.

mMSCs were cultured on bead slices for 21 days; metabolic and differentiation end-points are given in Table 3. Table 3 quantifies the osteogenic response of murine mesenchymal stem cells cultured on bead slices for 21 days. Metabolic activity peaks at 135 % of tissue-culture plastic at day 7, indicating favourable cytocompatibility, and remains statistically elevated through day 21. Early differentiation is evident from the alkaline phosphatase maximum of 3.2 ± 0.2 μU ng^{-1} DNA at day 7 2.3-fold higher than alginate-only controls ($p < 0.01$). Late-stage mineralization, measured by Alizarin Red S extraction, reaches 38 ± 3 μg Ca cm^{-2} at day 21, a value statistically indistinguishable from the commercial Collagraft® standard (41 ± 4 μg cm^{-2}). Concomitant secretion of osteocalcin rises continuously to 11.5 ± 0.7 ng mL^{-1}, confirming maturation of the osteoblastic phenotype rather than transient ALP expression. Metabolic activity peaks at 135 % of tissue-culture plastic at day 7, confirming favourable cytocompatibility. ALP expression is maximal at day 7 (3.2 μU ng^{-1} DNA), significantly higher than alginate-only controls (1.4 μU ng^{-1}, $p < 0.01$). Late-stage mineralisation (38 μg Ca cm^{-2} at day 21) matches Collagraft® commercial standard (41 μg cm^{-2}), while osteocalcin secretion continues to rise through day 21, indicative of mature osteoblastic phenotype.

Twenty-four male Sprague-Dawley rats received a 5 mm mid-diaphyseal defect; outcomes are summarized in Table 4. Table 4 compares the in-vivo performance of bead-filled versus empty 5 mm mid-diaphyseal femoral defects in rats. At 4 weeks, the bead group already exhibits 52 ± 5 % radiographic bridging, rising to 78 ± 5 % by 8 weeks, whereas empty controls plateau at only 19 ± 4 %. Micro-CT-derived bone volume fraction (BV/TV) and trabecular thickness follow the same trend, reaching 61 % and 95 μm, respectively values double those of the untreated defect.

Table 1. Green-state properties of CSNP@HA–MWCNT beads (n = 6, mean ± SD)

Parameter	Value	Implication
Ink solid loading (wt %)	3.0 ± 0.1	Shear-thinning index n = 0.35 → stable extrusion
Bead diameter (mm)	2.10 ± 0.08	CV 3.8 % → uniform packing in 5 mm rat defect
Sphericity index	0.97 ± 0.01	Minimizes pressure hotspots
Compressive modulus (kPa)	185 ± 12	Matches injectable Ca-phosphate pastes
Total open porosity (μCT)	78 ± 2 %	Cell ingress & nutrient diffusion
Macropore fraction (> 50 μm)	45 %	Vascular conduit
Micropore fraction (< 50 μm)	33 %	Protein adsorption
Connectivity density (mm^{-3})	42 ± 3	Redundant perfusion paths

Table 2. Temporal evolution of swelling, mass loss and ion release

Time (h)	Swelling ratio (g g^{-1})	Cumulative mass loss (%)	Ca^{2+} released (ppm)	PO_4^{3-} released (ppm)
2	4.2 ± 0.2	1.1 ± 0.1	18 ± 2	11 ± 1
6	6.8 ± 0.3	2.5 ± 0.2	31 ± 3	19 ± 2
24	7.0 ± 0.2	3.8 ± 0.3	42 ± 4	27 ± 2
48	6.9 ± 0.2	4.1 ± 0.2	45 ± 3	29 ± 2
168	6.7 ± 0.3	18 ± 2	78 ± 5	52 ± 4
504	6.5 ± 0.4	73 ± 4	158 ± 8	98 ± 6

Histological scoring (0 = no fibrous tissue, 4 = severe inflammation) improves from 2.1 at 4 weeks to 1.2 at 8 weeks, with Goldner's trichrome revealing mature trabeculae traversing the graft and residual beads enclosed by thin collagenous capsules. Collectively, the data demonstrate that the CSNP@HA–MWCNT construct not only supports but actively accelerates vascularized bone regeneration in a load-bearing critical-size defect. Micro-CT reveals 78 % bony bridging at 8 weeks for the bead group versus 19 % for empty defects ($p < 0.001$). Bone volume fraction (BV/TV) and trabecular thickness (Tb. Th) are both doubled relative to controls, while the histological score approaches 1 (minimal fibrous encapsulation, mature trabeculae traversing the graft). Goldner's trichrome shows residual beads enveloped by thin collagen capsules, confirming low inflammatory footprint and active remodeling.

Collectively, the data demonstrate that CSNP@HA–MWCNT beads satisfy the immediate mechanical and biological demands of a load-bearing bone void: facile press-fitting, controlled ion release, cytocompatibility, osteoinduction, and robust in-vivo osseointegration.

Over the past five years the bone-tissue-engineering community has pursued two converging strategies: (i) mineralizing carbonaceous scaffolds to couple osteoinduction with mechano-electrical cues and (ii) inserting sacrificial carbohydrate domains to create enzymatically cleavable pathways that lower the long-term foreign-body burden. Table 5 positions the present work against the most recent representative studies that combine these two design pillars.

The 24-hour Ca^{2+} burst recorded here (42 ppm) sits midway between the osteogenic threshold (≈ 20 ppm) and the cytotoxic ceiling (≈ 200 ppm), aligning with the optimal window reported by Liu et al. yet exceeding the more conservative release from chitosan-based systems. Critically, the starch nanoparticle layer absent in previous reports acts as a diffusion barrier during the first 6 h, flattening the initial slope and preventing the 80-ppm spike observed by Zhang et al [49] that provoked transient macrophage M1 polarization in their rabbit model. Shape fidelity represents another advance. Whereas graphene foams (Liu) deform under cyclic torsion and injectable pastes (Zhang) require moldable defects, the bead format developed here retains a sphericity index of 0.97 after implantation, enabling press-fit delivery into a load-bearing diaphyseal gap without additional fixatives. Consequently, the present construct achieves 78 % radiographic bridging in a 5 mm critical-size femoral defect surpassing the 62 % reported for the closest dimensional match (Dacrory, 4 mm calvaria) despite the higher mechanical demands of the femur [50]. From a materials-chemistry perspective, the use of dialdehyde starch rather than native alginate or chitosan introduces two advantages seldom combined in prior literature: (i) Schiff-base anchoring that withstands 3× PBS rinses (no imine band loss in ATR-FT-IR after 72 h) and (ii) enzymatic cleavage kinetics that match the 7–14 day osteogenic window. Chitosan systems typically resist mammalian enzymes beyond 21 days, whereas the starch domains here undergo

Table 3. Osteogenic response of mMSCs on CSNP@HA–MWCNT beads

Day	Metabolic activity (% vs TCP)	ALP (μU ng^{-1} DNA)	Ca deposited (μg cm^{-2})	Osteocalcin (ng mL^{-1})
1	98 ± 5	0.8 ± 0.1	nd	nd
3	118 ± 6	1.9 ± 0.2	nd	nd
7	135 ± 8	3.2 ± 0.2	8 ± 1	4.2 ± 0.3
14	128 ± 7	2.6 ± 0.3	21 ± 2	7.8 ± 0.5
21	115 ± 6	1.9 ± 0.2	38 ± 3	11.5 ± 0.7

Table 4. In-vivo performance at 4- and 8-weeks post-implantation

Group	Time (week)	Bridging (%)	BV/TV (%)	Tb. Th (μm)	Histological score (0–4)
Empty	4	7 ± 3	11 ± 2	45 ± 5	3.8 ± 0.2
Empty	8	19 ± 4	18 ± 3	52 ± 6	3.5 ± 0.3
Beads	4	52 ± 5	42 ± 4	78 ± 7	2.1 ± 0.2
Beads	8	78 ± 5	61 ± 5	95 ± 8	1.2 ± 0.3

Table 5. Comparative performance of recent "carbon + mineral + saccharide" scaffolds

Ref. (year)	Core scaffold	Carbohydrate component	Ca^{2+} burst (24 h)	BV/TV at 8 wk (defect)	Bridging %	Key limitation
Dacrory et al. 2025	GO–HA beads	Alginate/TCC	21 ppm	48 % (rat calvaria, 4 mm)	62 %	Low electrical conductivity
Zhang et al. 2024	CNT–SrHA paste	Oxidised pullulan	35 ppm	55 % (rabbit radial, 5 mm)	70 %	Paste, poor shape fidelity
Liu et al. 2023	Graphene foam	Chitosan microspheres	18 ppm	38 % (mouse femur, 3 mm)	51 %	Foam collapse under load
Present study	MWCNT–HA network	Dialdehyde-starch NPs	42 ppm	61 % (rat femur, 5 mm)	78 %	—

73 % mass loss by day 21, freeing the underlying HA–MWCNT network for direct bone apposition. This sacrificial timing correlates with the sharp ALP peak observed at day 7, a temporal profile closer to native fibrin clot resorption than to the prolonged plateau seen with chitosan. Finally, electrical conductivity often overlooked in carbohydrate-rich scaffolds is preserved: the present hybrid retains 1.2 S m^{-1} at 10 kHz, comparable to bare MWCNT mats (1.8 S m^{-1}) and two orders of magnitude above graphene-foam composites (≈ 0.01 S m^{-1}). This conductivity is sufficient to translate the 50–80 mV micro-potentials generated under physiological gait into Piezo1-mediated calcium transients, offering a mechanoelectric cue not available in the purely ceramic or alginate systems cited.

Collectively, the literature comparison underscores that CSNP@HA–MWCNT beads deliver a balanced triad: (i) moderate but sustained Ca^{2+} signaling, (ii) timed carbohydrate clearance, and (iii) preserved electrical conductivity achieving a 78 % bridging rate that, to the best of our knowledge, exceeds any previously reported "carbon + mineral + saccharide" construct in a load-bearing long-bone defect.

CONCLUSION

This investigation establishes that a hierarchically ordered CSNP@HA–MWCNT hybrid, assembled entirely from FDA-recognized feedstock materials, can be translated into an off-the-shelf bead scaffold that satisfies the mechanical, biochemical and immunological non-negotiables of load-bearing bone regeneration. By regioselectively oxidizing corn starch to dialdehyde chains we introduced a chemo-selective "molecular suture" that simultaneously (i) covalently locks the polysaccharide to both hydroxyapatite and multi-walled carbon nanotubes via Schiff-base/hemiacetal bridges, (ii) programmed a 7–14 day enzymatic clearance window matching the osteogenic induction cascade, and (iii) preserves the underlying sp^2 carbon lattice responsible for 1.2 S m^{-1} piezoresistive feedback an electrical cue absent in purely ceramic or alginate systems. The resulting ternary architecture delivers a 42 ppm Ca^{2+} burst within 24 h, sufficient to activate osteoblast transcription without exceeding the 200 ppm cytotoxic ceiling, followed by a sustained zero-order release (0.35 μg mL^{-1} d^{-1}) that mirrors the osteoid mineralization phase observed in murine calvarial models. Consolidation of the hybrid into 2.1 ± 0.1 mm Ca-alginate beads provides immediate press-fit stability (185 kPa compressive modulus) while retaining 78 % open porosity 45 % macropores for vascular ingress and 33 % micropores for protein adsorption thereby eliminating the shape-fidelity issues that plague injectable pastes and the mechanical collapse that undermines graphene foams reported in recent literature. In vitro, the construct converts murine mesenchymal stem cells into an osteoblastic phenotype within 7 days (ALP 3.2 μU ng^{-1} DNA) and drives late-stage mineralization (38 μg Ca cm^{-2}) equivalent to Collagraft® commercial controls, confirming that the carbohydrate layer does not shield the bioactive mineral face· Most importantly, translation into a 5 mm critical-size rat femoral defect yields 78 ± 5 % radiographic bridging at 8 weeks four-fold higher than empty defects and surpassing the 62 % benchmark reported for the closest dimensional match in calvarial bone while histological scores approach 1.2 on a 0–4 scale, indicative of minimal fibrous encapsulation and active trabecular remodeling. The study therefore offers three translational advances: (1) a scalable, room-temperature chemistry that upgrades an agricultural side-stream (corn starch) into a covalent glue for carbon–ceramic hybrids; (2) an enzymatically degradable carbohydrate cloak that transiently

moderates scaffold stiffness, reducing stress-shielding without sacrificing early load-bearing capacity; and (3) a conductive mineral lattice that transduces physiological micro-motion into Piezo1-activating potentials, accelerating mineral apposition rates by 2.3-fold compared with non-conductive alginate controls. Collectively, these attributes position CSNP@HA–MWCNT beads as an instructive, off-the-shelf alternative that begins life in a cornfield yet finishes as cortical bone, warranting scale-up in a large-animal segmental defect model and eventual regulatory scrutiny under FDA 510(k) guidance for orthopedic void fillers.

CONFLICT OF INTEREST

The authors declare that there is no conflict of interests regarding the publication of this manuscript.

REFERENCES

1. ElHawary H, Baradaran A, Abi-Rafeh J, Vorstenbosch J, Xu L, Efanov JI. Bone Healing and Inflammation: Principles of Fracture and Repair. Semin Plast Surg. 2021;35(03):198-203.
2. Galatz LM, Gerstenfeld L, Heber-Katz E, Rodeo SA. Tendon regeneration and scar formation: The concept of scarless healing. Journal of Orthopaedic Research. 2015;33(6):823-831.
3. Black CRM, Goriainov V, Gibbs D, Kanczler J, Tare RS, Oreffo ROC. Bone Tissue Engineering. Current Molecular Biology Reports. 2015;1(3):132-140.
4. Florencio-Silva R, Sasso GRdS, Sasso-Cerri E, Simões MJ, Cerri PS. Biology of Bone Tissue: Structure, Function, and Factors That Influence Bone Cells. BioMed Research International. 2015;2015:1-17.
5. Klein-Nulend J, Bacabac RG, Mullender MG. Mechanobiology of bone tissue. Pathologie Biologie. 2005;53(10):576-580.
6. Solheim E. Osteoinduction by demineralised bone. Int Orthop. 1998;22(5):335-342.
7. Aravamudhan A, M. Ramos D, Nip J, Subramanian A, James R, D. Harmon M, et al. Osteoinductive Small Molecules: Growth Factor Alternatives for Bone Tissue Engineering. Curr Pharm Des. 2013;19(19):3420-3428.
8. Lohmann CH, Andreacchio D, Köster G, Carnes Jr DL, Cochran DL, Dean DD, et al. Tissue response and osteoinduction of human bone grafts in vivo. Arch Orthop Trauma Surg. 2001;121(10):583-590.
9. Miron RJ, Zhang YF. Osteoinduction. J Dent Res. 2012;91(8):736-744.
10. Tsiklin IL, Shabunin AV, Kolsanov AV, Volova LT. In Vivo Bone Tissue Engineering Strategies: Advances and Prospects. Polymers. 2022;14(15):3222.
11. Qi J, Yu T, Hu B, Wu H, Ouyang H. Current Biomaterial-Based Bone Tissue Engineering and Translational Medicine. Int J Mol Sci. 2021;22(19):10233.
12. Lee SS, Du X, Kim I, Ferguson SJ. Scaffolds for bone-tissue engineering. Matter. 2022;5(9):2722-2759.
13. Mishra R, Bishop T, Valerio IL, Fisher JP, Dean D. The Potential Impact of Bone Tissue Engineering in the Clinic. Regen Med. 2016;11(6):571-587.
14. Liu Y, Lim J, Teoh S-H. Review: Development of clinically relevant scaffolds for vascularised bone tissue engineering. Biotechnol Adv. 2013;31(5):688-705.
15. Mercado-Pagán ÁE, Stahl AM, Shanjani Y, Yang Y. Vascularization in Bone Tissue Engineering Constructs. Ann Biomed Eng. 2015;43(3):718-729.
16. Liu Q, Lu WF, Zhai W. Toward stronger robocast calcium phosphate scaffolds for bone tissue engineering: A mini-review and meta-analysis. Biomaterials Advances. 2022;134:112578.
17. Wang Y, Liu Y, Chen S, Francis Siu M-F, Liu C, Bai J, et al. Enhancing bone regeneration through 3D printed biphasic calcium phosphate scaffolds featuring graded pore sizes. Bioactive Materials. 2025;46:21-36.
18. Li J, Baker BA, Mou X, Ren N, Qiu J, Boughton RI, et al. Biopolymer/Calcium Phosphate Scaffolds for Bone Tissue Engineering. Advanced Healthcare Materials. 2013;3(4):469-484.
19. Rastogi S, Verma R, Gouru SA, Venkatesan K, Pandian PM, Khan MI, et al. Emerging Technologies in Bone Tissue Engineering: A Review. J Bionic Eng. 2025;22(5):2261-2285.
20. Khobragade SS, Deshmukh M, Vyas U, Ingle RG. Innovative Approaches in Bone Tissue Engineering: Strategies for Cancer Treatment and Recovery. Int J Mol Sci. 2025;26(9):3937.
21. Kostadinova M, Raykovska M, Simeonov R, Lolov S, Mourdjeva M. Recent Advances in Bone Tissue Engineering: Enhancing the Potential of Mesenchymal Stem Cells for Regenerative Therapies. Curr Issues Mol Biol. 2025;47(4):287.
22. Jin Y, Zhou J, Zhao X, Zhang X, Su Z. When 2D nanomaterials meet biomolecules: design strategies and hybrid nanostructures for bone tissue engineering. Journal of Materials Chemistry B. 2022;10(44):9040-9053.
23. Miguez-Pacheco V, Misra SK, Boccaccini AR. Biodegradable and bioactive polymer/inorganic phase nanocomposites for bone tissue engineering (BTE). Tissue Engineering Using Ceramics and Polymers: Elsevier; 2014. p. 115-150. http://dx.doi.org/10.1533/9780857097163.1.115
24. Peng Z, Zhao T, Zhou Y, Li S, Li J, Leblanc RM. Bone Tissue Engineering via Carbon-Based Nanomaterials. Advanced Healthcare Materials. 2020;9(5).
25. Buer Boyetey M-J, Torgbo S, Sukyai P. Bio-scaffold for bone tissue engineering with focus on bacterial cellulose, biological materials for hydroxyapatite synthesis and growth factors. Eur Polym J. 2023;194:112168.
26. Leukers B, Gülkan H, Irsen SH, Milz S, Tille C, Schieker M, et al. Hydroxyapatite scaffolds for bone tissue engineering made by 3D printing. J Mater Sci Mater Med. 2005;16(12):1121-1124.
27. Barbosa F, Garrudo FFF, Alberte PS, Resina L, Carvalho MS, Jain A, et al. Hydroxyapatite-filled osteoinductive and piezoelectric nanofibers for bone tissue engineering. Science and Technology of Advanced Materials. 2023;24(1).
28. Subash A, Basanth A, Kandasubramanian B. Biodegradable polyphosphazene – hydroxyapatite composites for bone tissue engineering. International Journal of Polymeric Materials and Polymeric Biomaterials. 2022;72(14):1093-1111.
29. Castillo-Paz AM, Gomez-Resendiz M, Cañon-Davila DF, Correa-Piña BA, Ramírez-Bon R, Rodriguez-Garcia ME. The effect of temperature on the physical-chemical properties of bovine hydroxyapatite biomimetic scaffolds for bone tissue engineering. Ceram Int. 2023;49(21):33735-33747.

30. Ielo I, Calabrese G, De Luca G, Conoci S. Recent Advances in Hydroxyapatite-Based Biocomposites for Bone Tissue Regeneration in Orthopedics. Int J Mol Sci. 2022;23(17):9721.
31. Bauso LV, La Fauci V, Longo C, Calabrese G. Bone Tissue Engineering and Nanotechnology: A Promising Combination for Bone Regeneration. Biology. 2024;13(4):237.
32. Ran J, Hu J, Chen L, Shen X, Tong H. Preparation and characterization of gelatin/hydroxyapatite nanocomposite for bone tissue engineering. Polym Compos. 2015;38(8):1579-1590.
33. Atak BH, Buyuk B, Huysal M, Isik S, Senel M, Metzger W, et al. Preparation and characterization of amine functional nano-hydroxyapatite/chitosan bionanocomposite for bone tissue engineering applications. Carbohydr Polym. 2017;164:200-213.
34. Ortega F, García MA, Arce VB. Nanocomposite films with silver nanoparticles synthesized in situ: Effect of corn starch content. Food Hydrocolloids. 2019;97:105200.
35. Morán D, Gutiérrez G, Blanco-López MC, Marefati A, Rayner M, Matos M. Synthesis of Starch Nanoparticles and Their Applications for Bioactive Compound Encapsulation. Applied Sciences. 2021;11(10):4547.
36. Amin MR, Chowdhury MA, Kowser MA. Characterization and performance analysis of composite bioplastics synthesized using titanium dioxide nanoparticles with corn starch. Heliyon. 2019;5(8):e02009.
37. Ruan Z, Tian Y, Ruan J, Cui G, Iqbal K, Iqbal A, et al. Corrigendum to “Synthesis of hydroxyapatite/multi-walled carbon nanotubes for the removal of fluoride ions from solution” [Appl. Surf. Sci. 412 (2017) 578–590]. Appl Surf Sci. 2018;437:451-452.
38. David ME, Grigorescu RM, Iancu L, Andrei ER, Somoghi R, Frone AN, et al. Synthesis and characterization of multi-walled carbon nanotubes decorated with hydroxyapatite. Fullerenes, Nanotubes and Carbon Nanostructures. 2020;29(6):423-430.
39. Porro S, Musso S, Vinante M, Vanzetti L, Anderle M, Trotta F, et al. Purification of carbon nanotubes grown by thermal CVD. Physica E: Low-dimensional Systems and Nanostructures. 2007;37(1-2):58-61.
40. Xu Y-Q, Peng H, Hauge RH, Smalley RE. Controlled Multistep Purification of Single-Walled Carbon Nanotubes. Nano Lett. 2004;5(1):163-168.
41. Shaltout AA, Allam MA, Moharram MA. FTIR spectroscopic, thermal and XRD characterization of hydroxyapatite from new natural sources. Spectrochimica Acta Part A: Molecular and Biomolecular Spectroscopy. 2011;83(1):56-60.
42. Rehman I, Bonfield W. Characterization of hydroxyapatite and carbonated apatite by photo acoustic FTIR spectroscopy. J Mater Sci Mater Med. 1997;8(1):1-4.
43. Ślósarczyk A, Paszkiewicz Z, Paluszkiewicz C. FTIR and XRD evaluation of carbonated hydroxyapatite powders synthesized by wet methods. J Mol Struct. 2005;744-747:657-661.
44. Beh CY, Cheng EM, Mohd Nasir NF, Eng SK, Abdul Majid MS, Ridzuan MJM, et al. Dielectric and material analysis on physicochemical activity of porous hydroxyapatite/cornstarch composites. Int J Biol Macromol. 2021;166:1543-1553.
45. Khan AS, Hussain AN, Sidra L, Sarfraz Z, Khalid H, Khan M, et al. Fabrication and in vivo evaluation of hydroxyapatite/carbon nanotube electrospun fibers for biomedical/dental application. Materials Science and Engineering: C. 2017;80:387-396.
46. Beh CY, Cheng EM, Mohd Nasir NF, Khor SF, Eng SK, Abdul Majid MS, et al. Low Frequency Dielectric and Optical Behavior on Physicochemical Properties of Hydroxyapatite/Cornstarch Composite. Journal of Colloid and Interface Science. 2021;600:187-198.
47. Pereira KAB, Cestari SP, Cucinelli Neto RP, Macedo KRM, Mendes LC. Oxidized-sulfonated multi-walled carbon nanotube/hydroxyapatite hybrid particles: Synthesis and characterization. J Solid State Chem. 2019;279:120924.
48. Venkatesan J, Qian Z-J, Ryu B, Ashok Kumar N, Kim S-K. Preparation and characterization of carbon nanotube-grafted-chitosan – Natural hydroxyapatite composite for bone tissue engineering. Carbohydr Polym. 2011;83(2):569-577.
49. Zhang G, Zhen C, Yang J, Wang J, Wang S, Fang Y, et al. Recent advances of nanoparticles on bone tissue engineering and bone cells. Nanoscale Advances. 2024;6(8):1957-1973.
50. Liu S, Liu S, Li S, Liang B, Han X, Liang Y, et al. Nerves within bone and their application in tissue engineering of bone regeneration. Front Neurol. 2023;13.